

The Energy Spectrum of Ultra-High Energy Cosmic Rays across Declinations -90° to $+44.8^\circ$ as measured at the Pierre Auger Observatory

- A. Abdul Halim,¹ P. Abreu,² M. Aglietta,^{3,4} I. Allekotte,⁵ K. Almeida Cheminant,^{6,7} A. Almela,^{8,9} R. Aloisio,^{10,11} J. Alvarez-Muñiz,¹² A. Ambrosone,¹⁰ J. Ammerman Yebra,¹² G.A. Anastasi,^{13,14} L. Anchordoqui,¹⁵ B. Andrada,⁸ L. Andrade Dourado,^{10,11} S. Andringa,² L. Apollonio,^{16,17} C. Aramo,¹⁸ E. Arnone,^{19,4} J.C. Arteaga Velázquez,²⁰ P. Assis,² G. Avila,²¹ E. Avocone,^{22,11} A. Bakalova,²³ F. Barbato,^{10,11} A. Bartz Mocellin,²⁴ J.A. Bellido,¹ C. Berat,²⁵ M.E. Bertaina,^{19,4} M. Bianciotto,^{19,4} P.L. Biermann,²⁶ V. Binet,²⁷ K. Bismark,^{28,8} T. Bister,^{7,6} J. Biteau,^{29,30} J. Blazek,²³ J. Blümer,³¹ M. Boháčová,²³ D. Boncioli,^{22,11} C. Bonifazi,³² L. Bonneau Arbeletche,³³ N. Borodai,³⁴ J. Brack,³⁵ P.G. Brichetto Orchera,^{8,31} F.L. Briechle,³⁶ A. Bueno,³⁷ S. Buitink,³⁸ M. Buscemi,^{14,13} M. Büsken,^{28,8} A. Bwembya,^{7,6} K.S. Caballero-Mora,³⁹ S. Cabana-Freire,¹² L. Caccianiga,^{16,17} F. Campuzano,⁴⁰ J. Caraça-Valente,²⁴ R. Caruso,^{13,14} A. Castellina,^{3,4} F. Catalani,⁴¹ G. Cataldi,⁴² L. Cazon,¹² M. Cerda,⁴³ B. Čermáková,³¹ A. Cermenati,^{10,11} J.A. Chinellato,³³ J. Chudoba,²³ L. Chytka,⁴⁴ R.W. Clay,¹ A.C. Cobos Cerutti,⁴⁰ R. Colalillo,^{45,18} R. Conceição,² G. Consolati,^{17,46} M. Conte,^{47,42} F. Convenga,^{22,11} D. Correia dos Santos,⁴⁸ P.J. Costa,² C.E. Covault,⁴⁹ M. Cristinziani,⁵⁰ C.S. Cruz Sanchez,⁵¹ S. Dasso,^{52,53} K. Daumiller,³¹ B.R. Dawson,¹ R.M. de Almeida,⁴⁸ E.-T. de Boone,⁵⁰ B. de Errico,⁴⁸ J. de Jesús,^{8,31} S.J. de Jong,^{7,6} J.R.T. de Mello Neto,⁴⁸ I. De Mitri,^{10,11} J. de Oliveira,⁵⁴ D. de Oliveira Franco,⁵⁵ F. de Palma,^{47,42} V. de Souza,⁵⁶ E. De Vito,^{47,42} A. Del Popolo,^{13,14} O. Deligny,⁵⁷ N. Denner,²³ L. Deval,^{3,4} A. di Matteo,⁴ C. Dobrigkeit,³³ J.C. D'Olivo,⁵⁸ L.M. Domingues Mendes,^{59,2} Q. Dorostı,⁵⁰ J.C. dos Anjos,⁵⁹ R.C. dos Anjos,⁶⁰ J. Ebr,²³ F. Ellwanger,³¹ R. Engel,^{28,31} I. Epicoco,^{47,42} M. Erdmann,³⁶ A. Etchegoyen,^{8,9} C. Evoli,^{10,11} H. Falcke,^{7,61,6} G. Farrar,⁶² A.C. Fauth,³³ T. Fehler,⁵⁰ F. Feldbusch,⁶³ A. Fernandes,² M. Fernandez,⁶⁴ B. Fick,⁶⁵ J.M. Figueira,⁸ P. Filip,^{28,8} A. Filipčič,^{66,67} T. Fitoussi,³¹ B. Flaggs,⁶⁸ T. Fodran,⁷ A. Franco,⁴² M. Freitas,² T. Fujii,^{69,70} A. Fuster,^{8,9} C. Galea,⁷ B. García,⁴⁰ C. Gaudu,⁷¹ P.L. Ghia,⁵⁷ U. Giaccari,⁴² F. Gobbi,⁴³ F. Gollan,⁸ G. Golup,⁵ M. Gómez Berisso,⁵ P.F. Gómez Vitale,²¹ J.P. Gongora,²¹ J.M. González,⁵ N. González,⁸ D. Góra,³⁴ A. Gorgi,^{3,4} M. Gottowik,³¹ F. Guarino,^{45,18} G.P. Guedes,⁷² E. Guido,⁵⁰ L. Gültzow,³¹ S. Hahn,²⁸ P. Hamal,²³ M.R. Hampel,⁸ P. Hansen,⁵¹ V.M. Harvey,¹ A. Haungs,³¹ T. Hebbeker,³⁶ C. Hojvat,⁷³ J.R. Hörandel,^{7,6} P. Horvath,⁴⁴ M. Hrabovský,⁴⁴ T. Huege,^{31,38} A. Insolia,^{13,14} P.G. Isar,⁷⁴ M. Ismaiel,^{7,6} P. Janecek,²³ V. Jilek,²³ K.-H. Kampert,⁷¹ B. Keilhauer,³¹ A. Khakurdikar,⁷ V.V. Kizakke Covilakam,^{8,31} H.O. Klages,³¹ M. Kleifges,⁶³ J. Köhler,³¹ F. Krieger,³⁶ M. Kubatova,²³ N. Kunka,⁶³ B.L. Lago,⁷⁵ N. Langner,³⁶ N. Leal,⁸ M.A. Leigui de Oliveira,⁷⁶ Y. Lema-Capeans,¹² A. Letessier-Selvon,⁷⁷ I. Lhenry-Yvon,⁵⁷ L. Lopes,² J.P. Lundquist,⁶⁷ M. Mallamaci,^{78,14} D. Mandat,²³ P. Mantsch,⁷³ F.M. Mariani,^{16,17} A.G. Mariazzi,⁵¹ I.C. Mariş,⁶⁴ G. Marsella,^{78,14} D. Martello,^{47,42} S. Martinelli,^{31,8} M.A. Martins,¹² H.-J. Mathes,³¹ J. Matthews,⁷⁹ G. Matthiae,^{80,81} E. Mayotte,²⁴ S. Mayotte,²⁴ P.O. Mazur,⁷³ G. Medina-Tanco,⁵⁸ J. Meinert,⁷¹ D. Melo,⁸ A. Menshikov,⁶³ C. Merx,³¹ S. Michal,²³ M.I. Micheletti,²⁷ L. Miramonti,^{16,17} M. Mogarkar,³⁴ S. Mollerach,⁵ F. Montanet,²⁵ L. Morejon,⁷¹ K. Mulrey,^{7,6} R. Mussa,⁴ W.M. Namasaka,⁷¹ S. Negi,²³ L. Nellen,⁵⁸ K. Nguyen,⁶⁵ G. Nicora,⁸² M. Niechciol,⁵⁰ D. Nitz,⁶⁵ D. Nosek,⁸³ A. Novikov,⁶⁸ V. Novotny,⁸³ L. Nožka,⁴⁴ A. Nucita,^{47,42} L.A. Núñez,⁸⁴ J. Ochoa,^{8,31} C. Oliveira,⁵⁶ L. Östman,²³ M. Palatka,²³ J. Pallotta,⁸² S. Panja,²³ G. Parente,¹² T. Paulsen,⁷¹ J. Pawlowsky,⁷¹ M. Pech,²³ J. Pękala,³⁴ R. Pelayo,⁸⁵ V. Pelgrims,⁶⁴ L.A.S. Pereira,⁸⁶ E.E. Pereira Martins,^{28,8} C. Pérez Bertolli,^{8,31} L. Perrone,^{47,42} S. Petrera,^{10,11} C. Petrucci,²² T. Pierog,³¹ M. Pimenta,² M. Platino,⁸ B. Pont,⁷ M. Pourmohammad Shahvar,^{78,14} P. Privitera,⁶⁹ C. Priyadarshi,³⁴ M. Prouza,²³ K. Pytel,⁸⁷ S. Querchfeld,⁷¹ J. Rautenberg,⁷¹ D. Ravignani,⁸ J.V. Reginatto Akim,³³ A. Reuzki,³⁶ J. Ridky,²³ F. Riehn,^{12,88} M. Risse,⁵⁰ V. Rizi,^{22,11} E. Rodriguez,^{8,31} G. Rodriguez Fernandez,⁸¹ J. Rodriguez Rojo,²¹ S. Rossoni,⁵⁵ M. Roth,³¹ E. Roulet,⁵ A.C. Rovero,⁵² A. Saftoiu,⁸⁹ M. Saharan,⁷ F. Salamida,^{22,11} H. Salazar,⁹⁰ G. Salina,⁸¹ P. Sampathkumar,³¹ N. San Martin,²⁴ J.D. Sanabria Gomez,⁸⁴ F. Sánchez,⁸ E.M. Santos,⁹¹ E. Santos,²³ F. Sarazin,²⁴ R. Sarmento,² R. Sato,²¹ P. Savina,^{10,11} V. Scherini,^{47,42} H. Schieler,³¹ M. Schimassek,⁵⁷ M. Schimp,⁷¹ D. Schmidt,³¹ O. Scholten,^{38,92} H. Schoorlemmer,^{7,6} P. Schovánek,²³ F.G. Schröder,^{68,31} J. Schulte,³⁶ T. Schulz,²³ S.J. Sciutto,⁵¹ M. Scornavacche,^{8,31} A. Sedoski,⁸ A. Segreto,^{93,14} S. Sehgal,⁷¹ S.U. Shivashankara,⁶⁷ G. Sigl,⁵⁵ K. Simkova,^{38,64} F. Simon,⁶³ R. Šmídá,⁶⁹ P. Sommers,⁹⁴ R. Squartini,⁴³ M. Stadelmaier,^{31,17,16} S. Stanić,⁶⁷ J. Stasielak,³⁴ P. Stassi,²⁵ S. Stráhnz,²⁸ M. Straub,³⁶ T. Suomijärvi,²⁹ A.D. Supanitsky,⁸ Z. Svozilíkova,²³ K. Syrokvas,⁸³ Z. Szadkowski,⁸⁷ F. Tairli,¹ M. Tambone,^{45,18} A. Tapia,⁹⁵ C. Taricco,^{19,4} C. Timmermans,^{6,7} O. Tkachenko,²³ P. Tobiska,²³ C.J. Todero Peixoto,⁴¹ B. Tomé,² A. Travaini,⁴³ P. Travnicek,²³ M. Tueros,⁵¹ M. Unger,³¹ R. Uzeiroska,⁷¹ L. Vaclavek,⁴⁴ M. Vacula,⁴⁴ I. Vaiman,^{10,11} J.F. Valdés Galicia,⁵⁸ L. Valore,^{45,18} P. van Dillen,^{7,6} E. Varela,⁹⁰ V. Vašíčková,⁷¹ A. Vásquez-Ramírez,⁸⁴ D. Veberič,³¹ I.D. Vergara Quispe,⁵¹ S. Verpoest,⁶⁸ V. Verzi,⁸¹ J. Vicha,²³ J. Vink,⁹⁶ S. Vorobiov,⁶⁷ J.B. Vuta,²³ C. Watanabe,⁴⁸ A.A. Watson,⁹⁷ A. Weindl,³¹ M. Weitz,⁷¹ L. Wiencke,²⁴ H. Wilczyński,³⁴ B. Wundheiler,⁸ B. Yue,⁷¹ A. Yushkov,²³ E. Zas,¹² D. Zavrtanik,^{67,66} and M. Zavrtanik^{66,67}

(The Pierre Auger Collaboration)*

¹University of Adelaide, Adelaide, S.A., Australia

²Laboratório de Instrumentação e Física Experimental de Partículas – LIP and Instituto Superior Técnico – IST, Universidade de Lisboa – UL, Lisboa, Portugal

- ³Osservatorio Astrofisico di Torino (INAF), Torino, Italy
⁴INFN, Sezione di Torino, Torino, Italy
- ⁵Centro Atómico Bariloche and Instituto Balseiro (CNEA-UNCuyo-CONICET), San Carlos de Bariloche, Argentina
- ⁶Nationaal Instituut voor Kernfysica en Hoge Energie Fysica (NIKHEF), Science Park, Amsterdam, The Netherlands
⁷IMAPP, Radboud University Nijmegen, Nijmegen, The Netherlands
- ⁸Instituto de Tecnologías en Detección y Astropartículas (CNEA, CONICET, UNSAM), Buenos Aires, Argentina
⁹Universidad Tecnológica Nacional – Facultad Regional Buenos Aires, Buenos Aires, Argentina
¹⁰Gran Sasso Science Institute, L'Aquila, Italy
- ¹¹INFN Laboratori Nazionali del Gran Sasso, Assergi (L'Aquila), Italy
¹²Instituto Galego de Física de Altas Enerxías (IGFAE), Universidade de Santiago de Compostela, Santiago de Compostela, Spain
- ¹³Università di Catania, Dipartimento di Fisica e Astronomia "Ettore Majorana", Catania, Italy
¹⁴INFN, Sezione di Catania, Catania, Italy
- ¹⁵Department of Physics and Astronomy, Lehman College, City University of New York, Bronx, NY, USA
¹⁶Università di Milano, Dipartimento di Fisica, Milano, Italy
¹⁷INFN, Sezione di Milano, Milano, Italy
¹⁸INFN, Sezione di Napoli, Napoli, Italy
¹⁹Università Torino, Dipartimento di Fisica, Torino, Italy
- ²⁰Universidad Michoacana de San Nicolás de Hidalgo, Morelia, Michoacán, México
- ²¹Observatorio Pierre Auger and Comisión Nacional de Energía Atómica, Malargüe, Argentina
²²Università dell'Aquila, Dipartimento di Scienze Fisiche e Chimiche, L'Aquila, Italy
- ²³Institute of Physics of the Czech Academy of Sciences, Prague, Czech Republic
²⁴Colorado School of Mines, Golden, CO, USA
- ²⁵Univ. Grenoble Alpes, CNRS, Grenoble Institute of Engineering Univ. Grenoble Alpes, LPSC-IN2P3, 38000 Grenoble, France
²⁶Max-Planck-Institut für Radioastronomie, Bonn, Germany
- ²⁷Instituto de Física de Rosario (IFIR) – CONICET/U.N.R. and Facultad de Ciencias Bioquímicas y Farmacéuticas U.N.R., Rosario, Argentina
²⁸Karlsruhe Institute of Technology (KIT), Institute for Experimental Particle Physics, Karlsruhe, Germany
²⁹Université Paris-Saclay, CNRS/IN2P3, IJCLab, Orsay, France
³⁰Institut universitaire de France (IUF), France
- ³¹Karlsruhe Institute of Technology (KIT), Institute for Astroparticle Physics, Karlsruhe, Germany
³²International Center of Advanced Studies and Instituto de Ciencias Físicas, ECyT-UNSAM and CONICET, Campus Miguelete – San Martín, Buenos Aires, Argentina
- ³³Universidade Estadual de Campinas (UNICAMP), IFGW, Campinas, SP, Brazil
³⁴Institute of Nuclear Physics PAN, Krakow, Poland
³⁵Colorado State University, Fort Collins, CO, USA
- ³⁶RWTH Aachen University, III. Physikalisches Institut A, Aachen, Germany
³⁷Universidad de Granada and C.A.F.P.E., Granada, Spain
³⁸Vrije Universiteit Brussels, Brussels, Belgium
- ³⁹Universidad Autónoma de Chiapas, Tuxtla Gutiérrez, Chiapas, México
- ⁴⁰Instituto de Tecnologías en Detección y Astropartículas (CNEA, CONICET, UNSAM), and Universidad Tecnológica Nacional – Facultad Regional Mendoza (CONICET/CNEA), Mendoza, Argentina
- ⁴¹Universidade de São Paulo, Escola de Engenharia de Lorena, Lorena, SP, Brazil
⁴²INFN, Sezione di Lecce, Lecce, Italy
- ⁴³Observatorio Pierre Auger, Malargüe, Argentina
⁴⁴Palacky University, Olomouc, Czech Republic
- ⁴⁵Università di Napoli "Federico II", Dipartimento di Fisica "Ettore Pancini", Napoli, Italy
⁴⁶Politecnico di Milano, Dipartimento di Scienze e Tecnologie Aerospaziali , Milano, Italy
- ⁴⁷Università del Salento, Dipartimento di Matematica e Física "E. De Giorgi", Lecce, Italy
⁴⁸Universidade Federal do Rio de Janeiro, Instituto de Física, Rio de Janeiro, RJ, Brazil
⁴⁹Case Western Reserve University, Cleveland, OH, USA
- ⁵⁰Universität Siegen, Department Physik – Experimentelle Teilchenphysik, Siegen, Germany
⁵¹IFLP, Universidad Nacional de La Plata and CONICET, La Plata, Argentina
- ⁵²Instituto de Astronomía y Física del Espacio (IAFE, CONICET-UBA), Buenos Aires, Argentina
⁵³Departamento de Física and Departamento de Ciencias de la Atmósfera y los Océanos, FCEyN, Universidad de Buenos Aires and CONICET, Buenos Aires, Argentina
- ⁵⁴Instituto Federal de Educação, Ciência e Tecnologia do Rio de Janeiro (IFRJ), Brazil
⁵⁵Universität Hamburg, II. Institut für Theoretische Physik, Hamburg, Germany
- ⁵⁶Universidade de São Paulo, Instituto de Física de São Carlos, São Carlos, SP, Brazil
⁵⁷CNRS/IN2P3, IJCLab, Université Paris-Saclay, Orsay, France
- ⁵⁸Universidad Nacional Autónoma de México, México, D.F., México
- ⁵⁹Centro Brasileiro de Pesquisas Fisicas, Rio de Janeiro, RJ, Brazil
⁶⁰Universidade Federal do Paraná, Setor Palotina, Palotina, Brazil
- ⁶¹Stichting Astronomisch Onderzoek in Nederland (ASTRON), Dwingeloo, The Netherlands
⁶²New York University, New York, NY, USA

- ⁶³Karlsruhe Institute of Technology (KIT), Institut für Prozessdatenverarbeitung und Elektronik, Karlsruhe, Germany
⁶⁴Université Libre de Bruxelles (ULB), Brussels, Belgium
⁶⁵Michigan Technological University, Houghton, MI, USA
⁶⁶Experimental Particle Physics Department, J. Stefan Institute, Ljubljana, Slovenia
⁶⁷Center for Astrophysics and Cosmology (CAC), University of Nova Gorica, Nova Gorica, Slovenia
⁶⁸University of Delaware, Department of Physics and Astronomy, Bartol Research Institute, Newark, DE, USA
⁶⁹University of Chicago, Enrico Fermi Institute, Chicago, IL, USA
⁷⁰now at Graduate School of Science, Osaka Metropolitan University, Osaka, Japan
⁷¹Bergische Universität Wuppertal, Department of Physics, Wuppertal, Germany
⁷²Universidade Estadual de Feira de Santana, Feira de Santana, Brazil
⁷³Fermi National Accelerator Laboratory, Fermilab, Batavia, IL, USA
⁷⁴Institute of Space Science, Bucharest-Magurele, Romania
⁷⁵Centro Federal de Educação Tecnológica Celso Suckow da Fonseca, Petrópolis, Brazil
⁷⁶Universidade Federal do ABC, Santo André, SP, Brazil
⁷⁷Laboratoire de Physique Nucléaire et de Hautes Energies (LPNHE), Sorbonne Université, Université de Paris, CNRS-IN2P3, Paris, France
⁷⁸Università di Palermo, Dipartimento di Fisica e Chimica "E. Segrè", Palermo, Italy
⁷⁹Louisiana State University, Baton Rouge, LA, USA
⁸⁰Università di Roma "Tor Vergata", Dipartimento di Fisica, Roma, Italy
⁸¹INFN, Sezione di Roma "Tor Vergata", Roma, Italy
⁸²Laboratorio Atmósfera – Departamento de Investigaciones en Láseres y sus Aplicaciones – UNIDEF (CITEDEF-CONICET), Argentina
⁸³Charles University, Faculty of Mathematics and Physics,
Institute of Particle and Nuclear Physics, Prague, Czech Republic
⁸⁴Universidad Industrial de Santander, Bucaramanga, Colombia
⁸⁵Unidad Profesional Interdisciplinaria en Ingeniería y Tecnologías Avanzadas
del Instituto Politécnico Nacional (UPIITA-IPN), México, D.F., México
⁸⁶Universidade Federal de Campina Grande, Centro de Ciencias e Tecnologia, Campina Grande, Brazil
⁸⁷University of Lódź, Faculty of High-Energy Astrophysics, Lódź, Poland
⁸⁸now at Technische Universität Dortmund and Ruhr-Universität Bochum, Dortmund and Bochum, Germany
⁸⁹"Horia Hulubei" National Institute for Physics and Nuclear Engineering, Bucharest-Magurele, Romania
⁹⁰Benemérita Universidad Autónoma de Puebla, Puebla, México
⁹¹Universidade de São Paulo, Instituto de Física, São Paulo, SP, Brazil
⁹²also at Kapteyn Institute, University of Groningen, Groningen, The Netherlands
⁹³Istituto di Astrofisica Spaziale e Fisica Cosmica di Palermo (INAF), Palermo, Italy
⁹⁴Pennsylvania State University, University Park, PA, USA
⁹⁵Universidad de Medellín, Medellín, Colombia
⁹⁶Universiteit van Amsterdam, Faculty of Science, Amsterdam, The Netherlands
⁹⁷School of Physics and Astronomy, University of Leeds, Leeds, United Kingdom

(Dated: June 16, 2025)

The energy spectrum of cosmic rays above 2.5 EeV has been measured across the declination range $-90^\circ \leq \delta \leq +44.8^\circ$ using data from $\sim 310,000$ events accrued at the Pierre Auger Observatory from an exposure of $(104,900 \pm 3,100) \text{ km}^2 \text{ sr yr}$. No significant variations of energy spectra with declination are observed, after allowing or not for non-uniformities across the sky arising from the well-established dipolar anisotropies in the arrival directions of ultra-high energy cosmic rays. Additionally, the instep feature in the spectrum at $\simeq 10$ EeV reported previously is now established at a significance above 5σ . The quasi-uniformity of the energy spectrum across declinations disfavors an origin for the instep from a few distinctive sources.

I. INTRODUCTION

The discovery at the Pierre Auger Observatory [1] of a dipole in the distribution of cosmic rays of energy above 8 EeV of amplitude $\sim 6\%$ at a significance of over 5σ marks a significant advance in the field of high-energy cosmic-ray astronomy [2]. The status of this result is now 6.8σ , with an increase of the dipole amplitude with energy additionally identified [3]. Above 32 EeV, associations of high-energy cosmic rays with an overdensity in the Centaurus region, and with starburst galax-

ies, have been found, but only at the 4σ level [4]. Beyond 100 EeV, the arrival direction distribution across the whole sky, as derived from a combination of data from the Auger Observatory and the Telescope Array, is currently featureless [5]. It is thus important to examine whether the energy spectra vary with declination, particularly at the highest energies, where the new spectral feature near 10 EeV, identified in data from the Auger Observatory [6], indicates a two-step suppression of the spectrum [7, 8]. An analysis of spectra in bands of declination is presented below, exploiting the 1.2 m deep-water Cherenkov detectors of the Auger Observatory to obtain precision measurements over declinations -90° to $+44.8^\circ$.

As the zenith angle θ at impact of a primary cosmic-ray increases, the effects of the geomagnetic field on the distribu-

* spokespersons@auger.org; <http://www.auger.org>

tion of the muons in air showers become increasingly large so that the near-circular symmetry of signals around the shower axis found at low zenith angles is destroyed: above 70° , eccentricities over 0.9 are found. Accordingly, different methods of analyses are necessary for “vertical showers” ($\theta \leq 60^\circ$) and for the more “inclined events” (60° to 80°). The procedures for dealing with events with $\theta \leq 60^\circ$ were introduced nearly 65 years ago [9, 10]. Techniques to reconstruct events where the geomagnetic field is important were developed more recently, first to deal with measurements made at the Haverah Park array [11], with the methods later adapted for use with data from the Auger Observatory. The analysis used by the Auger Collaboration to obtain the energy of the primary particle for vertical showers is based on the determination of the signal in the water-Cherenkov detectors, $S(1000)$, interpolated at 1000 m from the centre of the shower [12], while for inclined events a parameter based on the number of muons in the shower, N_{19} , has been adopted [13, 14]. $S(1000)$ and N_{19} are subsequently converted into size parameters S_{38} and N_{68} , independent of the zenith angle, using the constant intensity method [6, 15], and the energies of events are finally derived by calibrating the size parameters using high-quality fluorescence measurements, obtained on clear, moonless nights, to provide calorimetric estimates of primary energies. Derivation of the energy spectrum from data with $\theta \leq 60^\circ$ requires no assumptions about features of hadronic interactions at high energies, or of the mass of the primary cosmic rays [6]. Minimal assumptions about these parameters are required for the inclined events as discussed in [16, 17].

The data used in the present analysis were recorded between 1 January 2004 and 31 December 2022. For vertical events the exposure was $\mathcal{E}_{[0-60^\circ]} = (81,100 \pm 2,400) \text{ km}^2 \text{ sr yr}$, with 279,131 events recorded above 2.5 EeV, while for inclined showers 31,543 events above 4 EeV were recorded in an exposure of $\mathcal{E}_{[60^\circ-80^\circ]} = (23,800 \pm 700) \text{ km}^2 \text{ sr yr}$. Exposures are independent of energy above these thresholds [6, 16], which are not identical mainly due to the attenuation of the electromagnetic cascade at high zenith angles.

II. COMBINATION OF INDIVIDUAL SPECTRA

Given the latitude of the Observatory, $\lambda \simeq -35.2^\circ$ and the zenith angle ranges mentioned in the previous section, the S_{38} -based dataset covers the range of declinations $-90^\circ \leq \delta \leq +24.8^\circ$ in equatorial coordinates, whereas the N_{68} one covers $-84.8^\circ \leq \delta \leq +44.8^\circ$. Our aim is to measure the energy spectrum over the whole declination range covered with the surface array, $-90^\circ \leq \delta \leq +44.8^\circ$. To do so, the independent spectra from the S_{38} - and N_{68} -based analyses, pertaining to complementary zenithal ranges and shown as the circles and squares respectively in the top panel of Fig. 1, must be combined.

The combination procedure follows from that presented in [18]. As with the individual spectra, the combined spectrum is obtained by forward-folding the effects of the finite energy accuracy of the detector into a proposed function tailored to

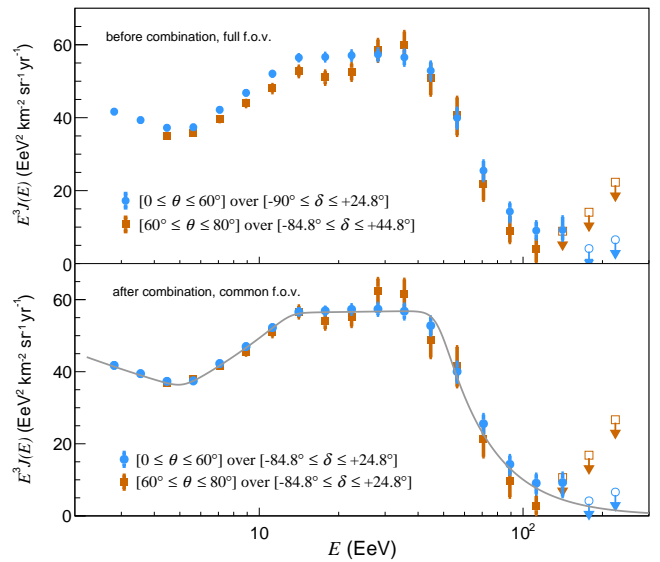


Figure 1. Individual energy spectra scaled by E^3 inferred from S_{38} - and N_{68} -based analyses before (top panel) and after (bottom panel) correcting the energies of inclined events to a best-fit common energy scale. The declination range after combination is reduced to $[-84.8^\circ, +24.8^\circ]$ to guarantee observation of the same sky. Upper limits at 90% confidence level are shown in empty bins. The gray line is the best-fit to data points after combination.

describe a series of power-law falloffs,

$$J(E; \mathbf{p}) = J_0 \left(\frac{E}{E_0} \right)^{-\gamma_0} \frac{\prod_{j=1}^3 \left[1 + \left(\frac{E}{E_{jk}} \right)^{\omega_{jk}^{-1}} \right]^{(\gamma_j - \gamma_k) \omega_{jk}}}{\prod_{j=1}^3 \left[1 + \left(\frac{E_0}{E_{jk}} \right)^{\omega_{jk}^{-1}} \right]^{(\gamma_j - \gamma_k) \omega_{jk}}}, \quad (1)$$

with $k = j + 1$ and eight free parameters encompassed in \mathbf{p} , namely the overall normalization J_0 , four spectral indices γ_j and three energy turning points E_{jk} ; the parameters ω_{jk} that govern the width of the transition from γ_j to γ_k are fixed to $\omega_{jk} = 0.05$ [6]; the pivot energy is chosen as $E_0 = 10^{0.5}$ EeV. The parameters \mathbf{p} are adjusted to obtain the best match between the observed number of events n_i in each differential energy bin of width $\Delta \log_{10} E = 0.1$ and the expected ones $v_i(\mathbf{p})$ simultaneously for both data streams. The minimization procedure is based on the product of Poissonian likelihood functions pertaining to each individual spectrum, $\mathcal{L}_{[0-60^\circ]}$ and $\mathcal{L}_{[60^\circ-80^\circ]}$.

Both individual spectra are subject to systematic uncertainties, which receive contributions from the absolute energy scale (14%) [19], the exposure (3%) [20], the unfolding procedure ($\leq 2\%$) [16] and the energies inferred from S_{38} and N_{68} ($\leq 3\%$) [6, 14]. No indication of further systematics has been found from a comparison of the spectra calculated over different time periods, seasons and ranges of zenith angle.

Most of the systematic uncertainties relating to each S_{38} - and N_{68} -based analysis are common to both. The notable exception concerns those inherited from the energy-calibration procedure that are, by essence, uncorrelated as the datasets used to calibrate S_{38} and N_{68} are independent. The largest

uncertainties are related to the calibration of N_{68} , as it is based on 605 events compared to 4,703 for S_{38} . Therefore, our strategy for the combination is to correct the energies of the N_{68} -based dataset, originally determined as $E = AN_{68}^B$, to a best-fit common energy scale, using two absolute departure parameters δA and δB so that $E' = (A + \delta A)N_{68}^{B+\delta B}$. It turns out that neglecting the systematic uncertainties in the energy scale of the S_{38} -based dataset is sufficient, as shown below, to get a statistically-meaningful combination.

In addition, as explained in the End Matter, the energy-calibration relationship of N_{68} may be affected by (logarithmic) non-linearities above ~ 10 EeV due to the sensitivity of N_{68} to the small, yet sharp, changes in mass composition recently uncovered [21, 22] and to experimental effects. A third departure parameter, δC , is therefore introduced so that the correction reads $E'' = (A + \delta A)N_{68}^{B+\delta B+\delta C}$ above 10 EeV. We show in the End Matter that the various sources of systematic uncertainties in N_{68} and in the relationship between N_{68} and energy can contribute to a non-linearity budget of $\sigma_C = 3 \times 10^{-2}$.

During each step of the fit, the energy-bin boundaries of the N_{68} -based analysis are corrected by varying the extra-parameters $\mathbf{x} = (\delta A, \delta B, \delta C)$ that govern the uncorrelated systematic uncertainties. Correspondingly, an extra-term in the joint likelihood restricts the values of the extra-parameters within their uncertainties. It is constructed by considering on the one hand the sum of two random variables δB and δC , and on the other hand the correlation between δA and δB . The log-likelihood function therefore stems from the convolution of a 2D Gaussian with correlation parameter $\rho \simeq -0.66$ with a 1D Gaussian pertaining to δC alone,

$$-2\ln \mathcal{L}_{\mathbf{x}}(\delta A, \delta B, \delta C) = \frac{\delta A^2(\sigma_B^2 + \sigma_C^2) - 2\rho\delta A\delta B\sigma_A\sigma_B + (\delta B + \delta C)^2\sigma_A^2}{\sigma_A^2(\sigma_C^2 + \sigma_B^2(1 - \rho^2))}, \quad (2)$$

with $\sigma_A \simeq 6 \times 10^{-2}$ EeV and $\sigma_B = 1.4 \times 10^{-2}$. In this way, for unrealistic changes in $(\delta A, \delta B, \delta C)$, the $-2\ln \mathcal{L}_{\mathbf{x}}(\delta A, \delta B, \delta C)$ term acts as a penalty factor while minimizing the total log-likelihood function $-2\ln \mathcal{L}(\mathbf{p}, \mathbf{x})$, which, overall, reads as

$$\mathcal{L}(\mathbf{p}, \mathbf{x}) = \mathcal{L}_{[0-60^\circ]}(\mathbf{p}, \mathbf{x}) \times \mathcal{L}_{[60^\circ-80^\circ]}(\mathbf{p}, \mathbf{x}) \times \mathcal{L}_{\mathbf{x}}(\mathbf{x}). \quad (3)$$

The outcome of the forward-folding fit is the set of parameters \mathbf{p} , and \mathbf{x} , that allows us to calculate ν_i and μ_i , which are the expected number of events including and not including the detector effects, respectively. Unfolding factors, defined as $c_i = \mu_i/\nu_i$, are then applied to correct for bin-to-bin migration effects induced by the finite accuracy of the response functions, which are determined in a data-driven manner as in [6] and given in the Supplemental material. The resulting spectral point for each energy bin is obtained as

$$J_i = \frac{c_i n_{i[0-60^\circ]} + c_i n_{i[60^\circ-80^\circ]}}{\mathcal{E}_i \Delta E_i}, \quad (4)$$

with $\mathcal{E}_i = \mathcal{E}_{[0-60^\circ]}$ for $0.4 \leq \log_{10}(E/\text{EeV}) \leq 0.6$ and $\mathcal{E}_i = \mathcal{E}_{[0-60^\circ]} + \mathcal{E}_{[60^\circ-80^\circ]}$ for $\log_{10}(E/\text{EeV}) \geq 0.6$. The minimization procedure, applied only to the events contained in the declination band $[-84.8^\circ, +24.8^\circ]$, common to both datasets, to

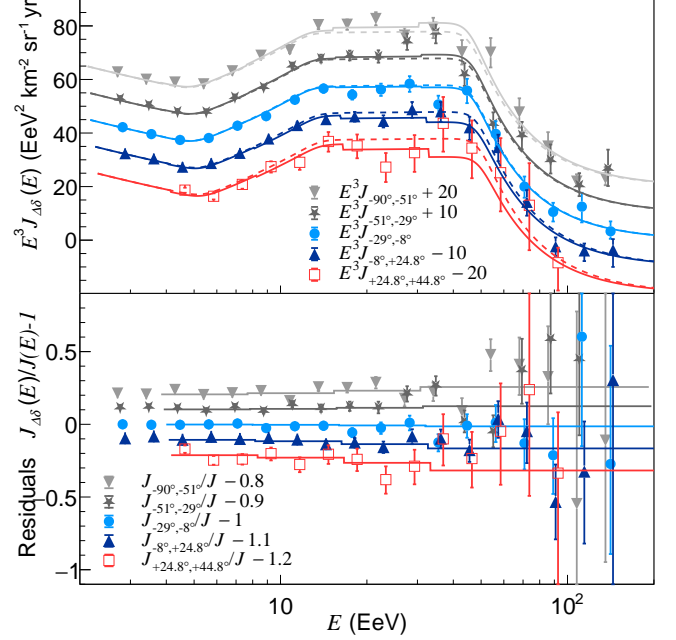


Figure 2. Top: Energy spectra in five declination ranges. The dotted reference lines are the best-fit function for the spectrum combined over $[-84.8^\circ, +24.8^\circ]$; the full ones account for the impact of dipole anisotropies in each band. Bottom: Corresponding residuals. Artificial shifts are applied for visualization purpose. An alternative view of the residuals is provided in the Supplemental material.

guarantee observation of the same sky so that spectra must be in statistical agreement, yields values of $\delta A/A \simeq (3.0 \pm 0.6)\%$, $\delta B/B \simeq (0.3 \pm 1.5)\%$, respectively corresponding to shifts of $2.6 \sigma_A$ and $0.2 \sigma_B$, and $\delta C \simeq (-2.0 \pm 2.0) \times 10^{-2}$. The resulting spectra are displayed in the bottom panel of Fig. 1. The most significant changes are in the lower energy bins, where the statistical power is greatest. Note that, as the analysis is actually designed so that $\mathcal{L}_{[0-60^\circ]}(\mathbf{p}, \mathbf{x})$ is independent of \mathbf{x} , the changes impact dominantly the N_{68} -based spectrum. The combined spectrum obtained with eqn. 4 shows a deviance of $D = 40.5$, which, if considered to follow a “C statistics” [23], can be compared to the expectation of $\langle D \rangle = 26.9 \pm 7.0$ to yield a p-value of $\simeq 0.12$.

III. SEARCHES FOR DECLINATION DEPENDENCES

We use in this section the best-fit parameters for $(\delta A, \delta B, \delta C)$ that allow for statistical agreement of spectra in the declination range $[-84.8^\circ, +24.8^\circ]$ to search for declination dependences over $[-90^\circ, +44.8^\circ]$. In particular, it is of interest to characterize the spectrum in the northernmost band $[+24.8^\circ, +44.8^\circ]$, where only inclined events are available (5,632 events after energy corrections from an exposure of $(4,100 \pm 120) \text{ km}^2 \text{ sr yr}$).

Detailed comparisons of the spectra in five declination bands are shown in Fig. 2. In addition to the northernmost one forementioned, four declination ranges are chosen with similar

Table I. Spectral parameters \mathbf{p} in several declination bands: normalization J_0 in $\text{km}^{-2} \text{sr}^{-1} \text{yr}^{-1} \text{EeV}^{-1}$ units, indices γ_j and break energies E_{jk} in EeV units; and probabilities $P(\geq Q^2)$ that $\mathbf{p}_{\Delta\delta}$ departs from \mathbf{p}_{ref} measured across $[-84.8^\circ, +24.8^\circ]$. In the declination band $[+24.8^\circ, +44.8^\circ]$, the threshold of the N_{68} -based analysis does not allow for measuring γ_1 and E_{12} , which are fixed to their value found across $[-84.8^\circ, +24.8^\circ]$.

$[\delta_{\min}, \delta_{\max}]$	J_0	γ_1	γ_2	γ_3	γ_4	E_{12}	E_{23}	E_{34}	$P(\geq Q^2)$
$[-84.8^\circ, +24.8^\circ]$	1.271 ± 0.004	3.26 ± 0.01	2.51 ± 0.03	2.99 ± 0.03	5.3 ± 0.2	5.1 ± 0.1	13 ± 1	48 ± 2	—
$[-90^\circ, -51^\circ]$	1.278 ± 0.007	3.24 ± 0.02	2.54 ± 0.06	3.18 ± 0.06	7.2 ± 1.0	5.1 ± 0.2	17 ± 2	62 ± 4	23%
$[-51^\circ, -29^\circ]$	1.281 ± 0.007	3.26 ± 0.02	2.46 ± 0.06	2.87 ± 0.06	4.6 ± 0.4	5.2 ± 0.2	12 ± 2	39 ± 4	13%
$[-29^\circ, -8^\circ]$	1.257 ± 0.007	3.28 ± 0.02	2.54 ± 0.06	3.02 ± 0.06	5.6 ± 0.4	4.9 ± 0.2	13 ± 2	49 ± 4	71%
$[-8^\circ, +24.8^\circ]$	1.266 ± 0.007	3.26 ± 0.02	2.50 ± 0.06	2.97 ± 0.06	6.1 ± 0.4	5.1 ± 0.2	12 ± 2	51 ± 4	34%
$[+24.8^\circ, +44.8^\circ]$	1.26 ± 0.03	3.26 (fixed)	2.6 ± 0.2	3.0 ± 0.2	11 ± 10	5.1 (fixed)	13 ± 4	69 ± 20	53%

exposures. In the top panel, individual spectra are shown and compared with the best-fit function (dotted lines) for the spectrum combined over $[-84.8^\circ, +24.8^\circ]$ and with the same best-fit function (full lines) taking into account the variation of the dipole amplitude with energy and declination as measured above 4 EeV. Because the energy-spectrum estimator is based primarily on the observed number of events through the directional exposure function $\omega(\delta)$, the expression of $J_{\Delta\delta}(E; \mathbf{p})$ is obtained as [6],

$$J_{\Delta\delta}(E; \mathbf{p}) = J(E; \mathbf{p}) \left(1 + \frac{\mathcal{E}_0 \int_{\Delta\delta} d\delta \cos \delta \omega(\delta) + d_z(E) \int_{\Delta\delta} d\delta \cos \delta \sin \delta \omega(\delta)}{\mathcal{E}_{\Delta\delta} \int d\delta \cos \delta \omega(\delta) + d_z(E) \int d\delta \cos \delta \sin \delta \omega(\delta)} \right), \quad (5)$$

with \mathcal{E}_0 the total exposure over the declination range of reference $[-84.8^\circ, +24.8^\circ]$, $\mathcal{E}_{\Delta\delta}$ that over the declination band under consideration, and where the integrations in the denominator are carried out over $[-84.8^\circ, +24.8^\circ]$. The coefficients $d_z(E)$ read $\{-0.013, -0.031, -0.070\}$ in differential bins of width $\Delta \log_{10} E = 0.3$ between 4 and 32 EeV and -0.13 above 32 EeV [3]. In the bottom panel, the best-fit function over $[-84.8^\circ, +24.8^\circ]$ is taken as a reference and the residual differences from this spectrum are plotted and compared with expectations. The residuals are observed to follow the trend imprinted by the dipole between 4 and 32 EeV; large statistical fluctuations dominate above 32 EeV.

Spectral parameters for each declination band, $\mathbf{p}_{\Delta\delta}$, are obtained by applying the combination procedure, except in the northernmost band where only inclined events contribute: they are listed in Table I. A quantitative statement on the statistical agreement between $\mathbf{p}_{\Delta\delta}$ and the reference parameters across $[-84.8^\circ, +24.8^\circ]$, \mathbf{p}_{ref} , can be drawn from the distance-squared quantity

$$Q^2 = (\mathbf{p}_{\Delta\delta} - \mathbf{p}_{\text{ref}})^T (\Sigma_{\Delta\delta} + \Sigma_{\text{ref}})^{-1} (\mathbf{p}_{\Delta\delta} - \mathbf{p}_{\text{ref}}), \quad (6)$$

which accounts for the correlations between parameters through their respective covariance matrices $\Sigma_{\Delta\delta}$ and Σ_{ref} given in the Supplemental material. Note that some fraction of the uncertainty in the exposure may depend on the declination, due for instance to the tilt and the spatial extension of the array [24]. We conservatively allocate an uncertainty of $100 \text{ km}^2 \text{ sr yr}$ in the exposure of each declination band that propagates into an additional contribution to the uncertainty

in J_0 . The probability that the set of parameters $\mathbf{p}_{\Delta\delta}$ departs from the reference ones is obtained by drawing at random mock samples and by counting the fraction of them displaying a value Q^2 larger than that in data. No significant departure is observed.

We note that some departure in γ_3 , E_{34} and γ_4 , which shape the spectrum at the highest energies, can be observed in the band $[-51^\circ, -29^\circ]$. Interestingly, this declination range encompasses the Centaurus region in which an overdensity over a circular region of $\simeq 24^\circ$ is present [4] and which has attracted much attention in, e.g., [25–30]. We have estimated the spectral features by restricting further, within the declination band, the region of interest within $\simeq 24^\circ$ around the position (right ascension $\alpha = 201^\circ$, declination $\delta = -43^\circ$) to check whether the harder values of γ_3 and γ_4 as well as the smaller value of E_{34} than everywhere else can be attributed to the overdensity. Large statistical fluctuations, however, prevent us from drawing any statement, given that $\gamma_3 = 2.8 \pm 0.3$, $E_{34} = (67 \pm 11)$ EeV and $\gamma_4 = 9 \pm 4$ in that specific region. The same conclusion holds about other, more modest, overdensities over the same scale that have attracted some attention in the literature [27, 29, 31, 32]: $\gamma_3 = 2.9 \pm 0.2$, $E_{34} = (41 \pm 11)$ EeV and $\gamma_4 = 5 \pm 1$ around the region of NGC 253 ($\alpha = 11.9^\circ, \delta = -25.3^\circ$), and, within the declination band $[-8^\circ, +24.8^\circ]$, $\gamma_3 = 3.3 \pm 0.3$, $E_{34} = (58 \pm 18)$ EeV and $\gamma_4 = 5 \pm 1$ around the region of NGC 1068 galaxy ($\alpha = 40.5^\circ, \delta = 0^\circ$). On the other hand, we also note that the spectral parameters of the northernmost declination band, also observed using Telescope Array with an exposure $\simeq 20\%$ larger [33], do not show deviations with respect to those of the reference band.

We conclude, consistent with large-scale anisotropy measurements [3], and consistent with our previous report limited to an exposure of $60,400 \text{ km}^2 \text{ sr yr}$ and to declinations from -90° to $+24.8^\circ$ [7], that the energy spectra are identical to within a mild dipolar modulation with declination from -90° to $+44.8^\circ$.

IV. SPECTRUM ACROSS DECLINATIONS -90° TO $+44.8^\circ$

Given the statistical agreement of the spectra with declinations, we present in Fig. 3 the combined spectrum across declinations -90° to $+44.8^\circ$, scaled by E^2 (energy flux). The colored band shows the systematic uncertainties, which have

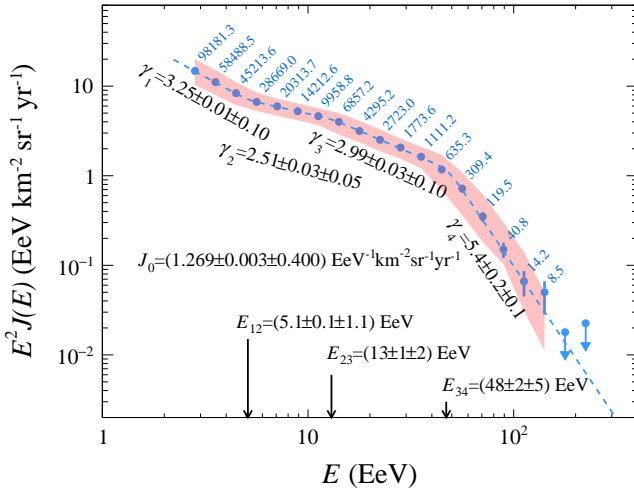


Figure 3. Energy spectrum scaled by E^2 (energy flux) across declinations $[-90^\circ, +44.8^\circ]$. The number of events corrected for detector effects is indicated in each bin. The red band stands for the systematic uncertainties while the dotted line for the best-fit function described by the spectral features given with their statistical and systematic uncertainties.

been propagated by repeating the analysis on datasets obtained by randomly sampling the different sources of systematics that affect individual energies and exposure. The main contribution stems, by far, from the 14% uncertainty in energy scale. The various spectral features, with their statistical and systematic uncertainties, are given in the figure. The data are also listed on a point-by-point basis in the Supplemental material.

Beyond the well-known features of the ankle and the steepening, evidence for the recently uncovered “instep” [6] is reinforced with this measurement. We had previously disfavored, with 3.9σ confidence, a model of the energy spectrum consisting of a series of two power laws followed by a slow suppression [6]. By drawing at random mock samples of observed energies following this reference model without instep, and by reconstructing the corresponding spectra using the reference model and the alternative one (eqn. 1), we build the distribution of the test statistics t from the ratio of the likelihood values associated to each hypothesis. Only two out of 10^8 realizations show a test statistic greater than the actual one (observed to be $t \approx 38$). This enables us, for 1-sided Gaussian distributions, to reject the reference model at the 5.5σ confidence level. The significance remains above 5.5σ when the complete chain of analysis is repeated with the energy scale adjusted by $\pm 14\%$ (the dominant systematic uncertainty) from the nominal one.

V. DISCUSSION

In this paper, we report for the first time the measurement of the energy spectrum of cosmic rays over the entire range of declination covered by the surface array of the Pierre Auger Observatory with an exposure of $104,900 \text{ km}^2 \text{ sr yr}$. This is made possible by using independent spectra measured over

$[0, 60^\circ]$ and $[60^\circ, 80^\circ]$ combined through a forward-folding procedure that makes use of a unique function to describe the underlying spectrum. Statistical agreement is obtained by increasing the energies inferred from N_{68} values measured between 60° and 80° from $+2.9\%$ at 4 EeV to 3.1% at 10 EeV; the increase then slows down and energies are changed by -1% at 100 EeV. Such changes are consistent with the uncertainties in the energy assignments to N_{68} .

A search for a declination dependence is performed by comparing the energy spectrum in five declination ranges with that measured in the band $[-84.8^\circ, +24.8^\circ]$, which is commonly covered when measuring individual spectra between $[0, 60^\circ]$ and $[60^\circ, 80^\circ]$ in zenith angle. All spectra are found to be consistent with the reference one, apart from a mild modulation expected from a dipolar anisotropy previously uncovered [3]. In particular, this statement applies to the northernmost declination band $[+24.8^\circ, +44.8^\circ]$, where only inclined events are available.

The combination of the two individual measurements and the statistical agreement across declinations lead to the construction of the spectrum from -90° to $+44.8^\circ$ declinations, where the features of the ankle, the instep and the suppression are firmly established. Among those features, the significance of the instep, which was recently uncovered with 3.9σ confidence [6], has reached 5.5σ . The increase in significance is consistent with the increase in exposure, in particular with that provided by the data stream of inclined events.

The absence of declination dependencies disfavors that the origin of the instep feature may be attributed to the distinctive spectrum of one or a few foreground sources contributing significantly to the total intensity. By contrast, the steepening seems to reflect the interplay between the flux contributions of the helium and carbon-nitrogen-oxygen components from sources rather similar [7, 34]. This is inline with the narrow range of maximum rigidity at the sources that can be inferred from the succession of rather pure-composition components of nuclei above 10 EeV [35–37]. The improved sensitivity in mass-composition with the upgraded Observatory [38] will allow for characterizing further the instep and therefore for shedding more light on its origin.

Acknowledgments. The successful installation, commissioning, and operation of the Pierre Auger Observatory would not have been possible without the strong commitment and effort from the technical and administrative staff in Malargüe. We are very grateful to the following agencies and organizations for financial support:

Argentina – Comisión Nacional de Energía Atómica; Agencia Nacional de Promoción Científica y Tecnológica (ANPCyT); Consejo Nacional de Investigaciones Científicas y Técnicas (CONICET); Gobierno de la Provincia de Mendoza; Municipalidad de Malargüe; NDM Holdings and Valle Las Leñas; in gratitude for their continuing cooperation over land access; Australia – the Australian Research Council; Belgium – Fonds de la Recherche Scientifique (FNRS); Research Foundation Flanders (FWO), Marie Curie Action of the European Union Grant No. 101107047; Brazil – Conselho Nacional de Desenvolvimento Científico e Tecnológico (CNPq); Financiadora de Estudos e Projetos (FINEP); Fundação de Amparo

à Pesquisa do Estado de Rio de Janeiro (FAPERJ); São Paulo Research Foundation (FAPESP) Grants No. 2019/10151-2, No. 2010/07359-6 and No. 1999/05404-3; Ministério da Ciência, Tecnologia, Inovações e Comunicações (MCTIC); Czech Republic – GACR 24-13049S, CAS LQ100102401, MEYS LM2023032, CZ.02.1.01/0.0/0.0/0.0/16_013/0001402, CZ.02.1.01/0.0/0.0/18_046/0016010 and CZ.02.1.01/0.0/0.0/17_049/0008422 and CZ.02.01.01/00/22_008/0004632; France – Centre de Calcul IN2P3/CNRS; Centre National de la Recherche Scientifique (CNRS); Conseil Régional Ile-de-France; Département Physique Nucléaire et Corpusculaire (PNC-IN2P3/CNRS); Département Sciences de l’Univers (SDU-INSU/CNRS); Institut Lagrange de Paris (ILP) Grant No. LABEX ANR-10-LABX-63 within the Investissements d’Avenir Programme Grant No. ANR-11-IDEX-0004-02; Germany – Bundesministerium für Bildung und Forschung (BMBF); Deutsche Forschungsgemeinschaft (DFG); Finanzministerium Baden-Württemberg; Helmholtz Alliance for Astroparticle Physics (HAP); Helmholtz-Gemeinschaft Deutscher Forschungszentren (HGF); Ministerium für Kultur und Wissenschaft des Landes Nordrhein-Westfalen; Ministerium für Wissenschaft, Forschung und Kunst des Landes Baden-Württemberg; Italy – Istituto Nazionale di Fisica Nucleare (INFN); Istituto Nazionale di Astrofisica (INAF); Ministero dell’Università e della Ricerca (MUR); CETEMPS Center of Excellence; Ministero degli Affari Esteri (MAE), ICSC Centro Nazionale di Ricerca in High Performance Computing, Big Data and Quantum Computing, funded by European Union NextGenerationEU, reference code CN_00000013; México – Consejo Nacional de Ciencia y Tecnología (CONACYT) No. 167733;

Universidad Nacional Autónoma de México (UNAM); PAPIIT DGAPA-UNAM; The Netherlands – Ministry of Education, Culture and Science; Netherlands Organisation for Scientific Research (NWO); Dutch national e-infrastructure with the support of SURF Cooperative; Poland – Ministry of Education and Science, grants No. DIR/WK/2018/11 and 2022/WK/12; National Science Centre, grants No. 2016/22/M/ST9/00198, 2016/23/B/ST9/01635, 2020/39/B/ST9/01398, and 2022/45/B/ST9/02163; Portugal – Portuguese national funds and FEDER funds within Programa Operacional Factores de Competitividade through Fundação para a Ciência e a Tecnologia (COMPETE); Romania – Ministry of Research, Innovation and Digitization, CNCS-UEFISCDI, contract no. 30N/2023 under Romanian National Core Program LAPLAS VII, grant no. PN 23 21 01 02 and project number PN-III-P1-1.1-TE-2021-0924/TE57/2022, within PNCDI III; Slovenia – Slovenian Research Agency, grants P1-0031, P1-0385, I0-0033, N1-0111; Spain – Ministerio de Ciencia e Innovación/Agencia Estatal de Investigación (PID2019-105544GB-I00, PID2022-140510NB-I00 and RYC2019-027017-I), Xunta de Galicia (CIGUS Network of Research Centers, Consolidación 2021 GRC GI-2033, ED431C-2021/22 and ED431F-2022/15), Junta de Andalucía (SOMM17/6104/UGR and P18-FR-4314), and the European Union (Marie Skłodowska-Curie 101065027 and ERDF); USA – Department of Energy, Contracts No. DE-AC02-07CH11359, No. DE-FR02-04ER41300, No. DE-FG02-99ER41107 and No. DE-SC0011689; National Science Foundation, Grant No. 0450696, and NSF-2013199; The Grainger Foundation; Marie Curie-IRSES/EPLANET; European Particle Physics Latin American Network; and UNESCO.

-
- [1] A. Aab *et al.* (Pierre Auger), *Nucl. Instrum. Meth. A* **798**, 172 (2015), arXiv:1502.01323 [astro-ph.IM].
 - [2] A. Aab *et al.* (Pierre Auger), *Science* **357**, 1266 (2017), arXiv:1709.07321 [astro-ph.HE].
 - [3] A. A. Halim *et al.* (Pierre Auger), *Astrophys. J.* **976**, 48 (2024), arXiv:2408.05292 [astro-ph.HE].
 - [4] P. Abreu *et al.* (Pierre Auger), *Astrophys. J.* **935**, 170 (2022), arXiv:2206.13492 [astro-ph.HE].
 - [5] T. Fujii, PoS ICRC2023, 031 (2024), arXiv:2401.08952 [astro-ph.HE].
 - [6] A. Aab *et al.* (Pierre Auger), *Phys. Rev. D* **102**, 062005 (2020), arXiv:2008.06486 [astro-ph.HE].
 - [7] A. Aab *et al.* (Pierre Auger), *Phys. Rev. Lett.* **125**, 121106 (2020), arXiv:2008.06488 [astro-ph.HE].
 - [8] S. Razzaque, *APS Physics* **13**, 145 (2020).
 - [9] F. Scherb, M.I.T. Nuclear Science Technical Report **71** (1959).
 - [10] G. W. Clark, J. Earl, W. L. Kraushaar, J. Linsley, B. B. Rossi, F. Scherb, and D. W. Scott, *Phys. Rev.* **122**, 637 (1961).
 - [11] M. Ave, J. A. Hinton, R. A. Vazquez, A. A. Watson, and E. Zas, *Phys. Rev. Lett.* **85**, 2244 (2000), arXiv:astro-ph/0007386.
 - [12] A. Aab *et al.* (Pierre Auger), *JINST* **15** (10), P10021, arXiv:2007.09035 [astro-ph.IM].
 - [13] M. Ave, R. A. Vazquez, and E. Zas, *Astropart. Phys.* **14**, 91 (2000), arXiv:astro-ph/0011490.
 - [14] A. Aab *et al.* (Pierre Auger), *JCAP* **08**, 019 (2014), arXiv:1407.3214 [astro-ph.HE].
 - [15] J. Hersil, I. Escobar, D. Scott, G. Clark, and S. Olbert, *Phys. Rev. Lett.* **6**, 22 (1961).
 - [16] A. Aab *et al.* (Pierre Auger), *JCAP* **08**, 049 (2015), arXiv:1503.07786 [astro-ph.HE].
 - [17] H. P. Dembinski, P. Billoir, O. Deligny, and T. Hebbeker, *Astropart. Phys.* **34**, 128 (2010), arXiv:0904.2372 [astro-ph.IM].
 - [18] P. Abreu *et al.* (Pierre Auger), *Eur. Phys. J. C* **81**, 966 (2021), arXiv:2109.13400 [astro-ph.HE].
 - [19] V. Verzi (Pierre Auger), in *33rd International Cosmic Ray Conference* (2013) p. 0928.
 - [20] J. Abraham *et al.* (Pierre Auger), *Nucl. Instrum. Meth. A* **613**, 29 (2010), arXiv:1111.6764 [astro-ph.IM].
 - [21] A. Abdul Halim *et al.* (Pierre Auger), *Phys. Rev. Lett.* **134**, 021001 (2025), arXiv:2406.06315 [astro-ph.HE].
 - [22] A. Abdul Halim *et al.* (Pierre Auger), *Phys. Rev. D* **111**, 022003 (2025), arXiv:2406.06319 [astro-ph.HE].
 - [23] M. Bonamente, *J. Appl. Stat.* **47**, 2044 (2020), arXiv:1912.05444 [astro-ph.HE].
 - [24] P. Abreu *et al.* (Pierre Auger), *Astrophys. J. Suppl.* **203**, 34 (2012), arXiv:1210.3736 [astro-ph.HE].
 - [25] P. L. Biermann and V. de Souza, *Astrophys. J.* **746**, 72 (2012), arXiv:1106.0625 [astro-ph.HE].

- [26] A. Keivani, G. R. Farrar, and M. Sutherland, *Astropart. Phys.* **61**, 47 (2014), arXiv:1406.5249 [astro-ph.HE].
- [27] A. R. Bell and J. H. Matthews, *Mon. Not. Roy. Astron. Soc.* **511**, 448 (2022), arXiv:2108.08879 [astro-ph.HE].
- [28] S. Mollerach and E. Roulet, *Phys. Rev. D* **110**, 063030 (2024), arXiv:2406.19199 [astro-ph.HE].
- [29] S. Marafico, J. Biteau, A. Condorelli, O. Deligny, and J. Bregeon, *Astrophys. J.* **972**, 4 (2024), arXiv:2405.17179 [astro-ph.HE].
- [30] R. Mbarek, D. Caprioli, and K. Murase, *Phys. Rev. D* **111**, 023024 (2025), arXiv:2410.05696 [astro-ph.HE].
- [31] G. E. Romero, A. L. Müller, and M. Roth, *Astron. Astrophys.* **616**, A57 (2018), arXiv:1801.06483 [astro-ph.HE].
- [32] L. A. Anchordoqui and J. F. Soriano, *PoS ICRC2019*, 255 (2021), arXiv:1905.13243 [astro-ph.HE].
- [33] R. U. Abbasi et al. (Telescope Array), (2024), arXiv:2406.08612 [astro-ph.HE].
- [34] A. A. Halim et al. (Pierre Auger), *JCAP* **05**, 024, arXiv:2211.02857 [astro-ph.HE].
- [35] D. Ehlert, F. Oikonomou, and M. Unger, *Phys. Rev. D* **107**, 103045 (2023), arXiv:2207.10691 [astro-ph.HE].
- [36] G. R. Farrar, *Phys. Rev. Lett.* **134**, 081003 (2025), arXiv:2405.12004 [astro-ph.HE].
- [37] B. T. Zhang, K. Murase, N. Ekanger, M. Bhattacharya, and S. Horiuchi, (2024), arXiv:2405.17409 [astro-ph.HE].
- [38] A. Aab et al. (Pierre Auger), (2016), arXiv:1604.03637 [astro-ph.IM].
- [39] B. R. Dawson et al. (Pierre Auger), *EPJ Web Conf.* **197**, 01004 (2019).
- [40] V. M. Harvey et al. (Pierre Auger), *PoS ICRC2023*, 300 (2023).
- [41] J. Bellido et al. (Pierre Auger), *PoS ICRC2023*, 211 (2023).
- [42] A. Aab et al. (Pierre Auger), *Phys. Rev. D* **90**, 122005 (2014), arXiv:1409.4809 [astro-ph.HE].
- [43] J. Matthews, *Astropart. Phys.* **22**, 387 (2005).
- [44] T. Pierog, I. Karpenko, J. M. Katzy, E. Yatsenko, and K. Werner, *Phys. Rev. C* **92**, 034906 (2015), arXiv:1306.0121 [hep-ph].
- [45] L. Cazon, R. Conceição, and F. Riehn, *Phys. Lett. B* **784**, 68 (2018), arXiv:1803.05699 [hep-ph].

END MATTER

In this appendix, we first provide details of the energy-calibration of S_{38} and of N_{68} , and then explain the sources of energy-dependent systematic uncertainties in N_{68} that enter into the budget σ_C and justify the use of a non-zero δC above 10 EeV.

Table II. Coefficients of the second-degree polynomial in terms of $y_S = \log_{10}(S_{38}/(40 \text{ VEM}))$ for the parameters a_S , b_S and c_S .

	y_S^0	y_S^1	y_S^2
a_S	0.936	0.005	-0.400
b_S	-1.62	-0.51	-0.13
c_S	-0.92	0.54	1.75

The energy calibration of $S(1000)$ is derived from a two-step process [6]. Firstly, $S(1000)$ is corrected for attenuation effects with zenith angle θ by using the Constant Intensity Cut method [15]. For a given intensity threshold,

the attenuation curve is fitted with a third-degree polynomial, $S(1000) = S_{38}(1 + a_S x_S + b_S x_S^2 + c_S x_S^3)$, where $x_S = \cos^2 \theta - \cos^2 38^\circ$ and S_{38} is a zenith-independent shower-size estimator. The intensity-threshold dependence in the curves is accounted for by introducing an empirical dependence in terms of $y_S = \log_{10}(S_{38}/40 \text{ VEM})$ in the coefficients a_S , b_S and c_S through a second-order polynomial in y . The polynomial coefficients, updated with respect to those in [6], are given in Table II. They relate to S_{38} values ranging from 15 VEM to 120 VEM. Outside these bounds, the coefficients are set to their values at 15 and 120 VEM. Secondly, the corrected shower-size estimator, S_{38} , is converted into energy E using a power-law calibration relationship, $E = A_S(S_{38})^{B_S}$, determined with high-quality events detected simultaneously with the fluorescence detector. The energy scale is based on [39], with recent improvements concerning aerosol attenuation [40] and longitudinal-profile reconstruction [41]. In this study, $A_S = (1.86 \pm 0.03) \times 10^{-1} \text{ EeV}$ and $B_S = 1.021 \pm 0.004$.

Table III. Coefficients of the first-degree polynomial in terms of $y_N = \log_{10} N_{19}$ for the parameters a_N and b_N .

	y_N^0	y_N^1
a_N	-0.292	0.468
b_N	-4.96	0.79

The energy calibration of N_{19} is carried out in the same manner. A constant-intensity-cut correction is applied to the (relative) muon-number estimator N_{19} using a second-degree polynomial, $N_{19} = N_{68}(1 + a_N x_N + b_N x_N^2)$, which is enough to guarantee same intensity in bins of $\cos^2 \theta$ between 60° and 80° (with $x_N = \cos^2 \theta - \cos^2 68^\circ$). The intensity-threshold dependence is accounted for by introducing an empirical dependence in terms of $y_N = \log_{10}(N_{19})$ in the coefficients a_N and b_N . The polynomial coefficients are given in Table III. They relate to N_{68} values ranging from 0.9 to 4.5. Outside these bounds, the coefficients are set to their values at 0.9 and 4.5. The energy-calibration relationship is $E = A_N(N_{68})^{B_N}$, with $A_N = (5.29 \pm 0.06) \text{ EeV}$ and $B_N = 1.046 \pm 0.014$. Note that these values are referred to as $A \pm \sigma_A$ and $B \pm \sigma_B$ in the main text.

Since N_{68} depends on the mass composition of the primary particles, its calibration relationship to the energy measured with the fluorescence technique accounts for the trend of the composition change with energy inherently as the underlying mass distribution is directly sampled by the fluorescence detectors. The use of a single power law for the relationship between N_{68} and E is then justified only for a single logarithmic evolution of the composition as a function of energy. This turns out to be the case, within the statistical uncertainties of the fluorescence dataset, above $\simeq 2 \text{ EeV}$ [42]. However, using deep-neural-network techniques applied to the surface-detector dataset, sharp changes of the elongation rate, too small to show up within the statistics available with the

¹ A VEM corresponds to the energy deposit of one vertical equivalent muon.

fluorescence technique, have recently been uncovered around $\simeq 6$ EeV, $\simeq 10$ EeV and $\simeq 30$ EeV [21, 22]. The impact of these elongation rate changes on the energy calibration of N_{68} can be estimated as follows. Within the Heitler-Matthews superposition model of air shower [43], the number of muons N_μ increases with the cosmic-ray mass number A as $N_\mu \propto A^{1-\beta}$. Assuming that the slope of N_{68} with A follows that of N_μ , the change of slope of N_{68} , $\Delta m_{N_{68}}$, can be related to that of the shower maximum slant depth, $\Delta m_{X_{\max}}$ through

$$\Delta m_{N_{68}} = -\frac{1-\beta}{D_0} \Delta m_{X_{\max}}, \quad (7)$$

with $D_0 \simeq 56.1$ g cm $^{-2}$ the elongate rate of protons expected from EPOS-LHC [44]. Using $\beta \simeq 0.927$ as a benchmark [45], and considering to first order a single change of elongation rate around 10 EeV to describe the observed series of kinks from below 6 EeV to above 30 EeV, we get an amplitude for the expected non-linearity of N_{68} of $\simeq 2.5\%$ per decade. We note that we neglect here the correlated non-linearity effects in the energy calibration of S_{38} as they are smaller.

Another source of logarithmic non-linearities between N_{68} and E stems from the use of the constant-intensity-cut correction to make uniform the distribution of events in terms of $\sin^2 \theta$. The correction is necessary to compensate for imperfections of the N_{19} energy estimator, which accounts for muon contributions to the signals and requires model-dependent corrections for electromagnetic ones, not negligible between $\theta = 60^\circ$ and $\theta \simeq 70^\circ$. However, smaller, yet genuine, deviations of the $\sin^2 \theta$ distribution from uniformity, Δ , are expected in presence of dipolar anisotropies. They can be estimated as [24]

$$\Delta = \frac{N_{\text{dip}}}{N_{\text{iso}}} d_z \sin \lambda \cos \theta, \quad (8)$$

with N_{iso} (N_{dip}) the expected number of events in the covered region of the sky for an isotropic (a dipolar) angular distribution. While Δ is well within 1% for $\theta \leq 60^\circ$ for the dipole components d_z of interest (measured with large uncertainties, though), it increases up to, on average, $\simeq 3\%$ for $\theta \geq 60^\circ$. We estimated that the uniformity of the $\sin^2 \theta$ distribution forced by the constant intensity correction for $N_{68} < 4.5$ ($E \simeq 20$ EeV) can then lead to energy distortions of $\simeq 1.5\%$ between 4 and $\simeq 20$ EeV, while higher energies would not be impacted as the energy dependence of the polynomial coefficients relating N_{19} to N_{68} is frozen. This effectively acts as a source of non-linearity that occurs around $\simeq 20$ EeV.

Overall, we add in quadrature both sources of non-linearities and end up with $\sigma_C = 3 \times 10^{-2}$, and choose, as a first-order approximation, the transition energy at 10 EeV. We have checked that the best-fit value for δC is mildly impacted when increasing σ_C to 5×10^{-2} or increasing the transition energy.

SUPPLEMENTAL MATERIAL

We provide in this supplemental material a few summary plots and data related to the analysis presented in the article.

The response function for events between 0 and 60° is described in detail in our previous paper [6]. We have applied the same data-driven techniques to determine that for events between 60° and 80° . The resolution function is parameterized as a Gaussian function with σ_N parameter evolving with energy as

$$\frac{\sigma_N(E)}{E} = 0.046 + \frac{0.34}{\sqrt{E}}, \quad (9)$$

with E in EeV. No significant bias is found in the sub-threshold energy bins of interest, down to 2.5 EeV. The efficiency is described as (still with E in EeV)

$$\epsilon(E) = 0.5 \left(1 + \text{erf} \left(\frac{\log_{10} E}{0.34} \right) \right). \quad (10)$$

In Fig. 4, we present an alternative version of the bottom panel of Fig. 2. Here, the energy-spectra residuals in the five declination bands are zoomed within $\pm 25\%$ while no artificial shifts are applied for visualization purpose; some data points at high energies therefore lie outside the windows. The reference lines are the best-fit function for the spectrum combined over $[-84.8^\circ, +24.8^\circ]$ accounting for dipole anisotropies.

The correlation matrix relative to the covariance matrices used to search for differences in the spectral features is given in Table IV. It provides, together with the corresponding uncertainties in the parameters listed in Table I, the coefficients needed to get Σ_{ref} as well as $\Sigma_{\Delta\delta}$.

Finally, the combined spectrum data points with their statistical and systematic uncertainties are collected in Table V together with the observed and corrected number of events, while the correlation matrix of the spectrum data points that accounts for systematic uncertainties is given in Table VI.

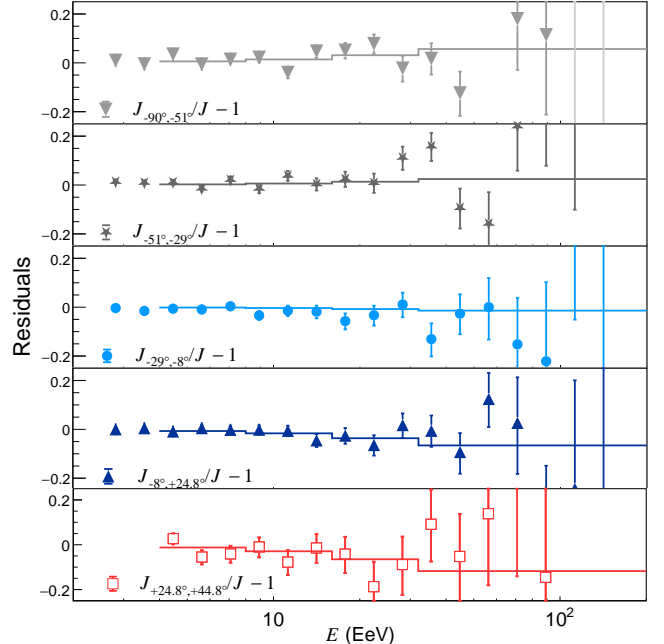


Figure 4. Energy-spectra residuals zoomed within $\pm 25\%$ in the five declination bands.

Table IV. Correlation matrix relative to Σ_{ref} expressed in a basis $(J_0, \gamma_1, E_{12}, \gamma_2, E_{23}, \gamma_3, E_{34}, \gamma_4)$.

1.000	-0.535	+0.613	-0.396	-0.162	+0.218	-0.182	-0.317
	1.000	-0.782	+0.494	+0.343	+0.111	+0.561	+0.512
		1.000	-0.872	-0.609	-0.186	-0.329	-0.303
			1.000	+0.827	+0.313	+0.104	+0.052
				1.000	+0.594	+0.007	-0.052
					1.000	+0.133	-0.186
						1.000	+0.431
							1.000

Table V. Combined spectrum data.

$\log_{10}(E/\text{EeV})$	$J(E) \pm \sigma_{\text{stat}}(E) \pm \sigma_{\text{syst}}(E) (\text{EeV}^{-1} \text{ km}^{-2} \text{ sr}^{-1} \text{ yr}^{-1})$	n	n_{corr}
0.45	$(1.8614 \begin{array}{l} +0.0065 \\ -0.0065 \end{array} \begin{array}{l} +0.7 \\ -0.6 \end{array}) \times 10^0$	107232	98178.2
0.55	$(8.808 \begin{array}{l} +0.040 \\ -0.040 \end{array} \begin{array}{l} +3.2 \\ -2.5 \end{array}) \times 10^{-1}$	61873	58483.8
0.65	$(4.183 \begin{array}{l} +0.022 \\ -0.022 \end{array} \begin{array}{l} +1.4 \\ -1.1 \end{array}) \times 10^{-1}$	48929	45207.8
0.75	$(2.107 \begin{array}{l} +0.014 \\ -0.014 \end{array} \begin{array}{l} +0.6 \\ -0.4 \end{array}) \times 10^{-1}$	30525	28678.2
0.85	$(1.186 \begin{array}{l} +0.009 \\ -0.009 \end{array} \begin{array}{l} +0.3 \\ -0.3 \end{array}) \times 10^{-1}$	20984	20314.9
0.95	$(6.590 \begin{array}{l} +0.059 \\ -0.059 \end{array} \begin{array}{l} +1.5 \\ -1.4 \end{array}) \times 10^{-2}$	14590	14213.9
1.05	$(3.668 \begin{array}{l} +0.039 \\ -0.039 \end{array} \begin{array}{l} +0.9 \\ -0.8 \end{array}) \times 10^{-2}$	10159	9957.9
1.15	$(2.001 \begin{array}{l} +0.024 \\ -0.026 \end{array} \begin{array}{l} +0.5 \\ -0.6 \end{array}) \times 10^{-2}$	6984	6858.1
1.25	$(9.982 \begin{array}{l} +0.015 \\ -0.017 \end{array} \begin{array}{l} +0.3 \\ -0.3 \end{array}) \times 10^{-3}$	4396	4296.4
1.35	$(5.027 \begin{array}{l} +0.097 \\ -0.101 \end{array} \begin{array}{l} +1.5 \\ -1.3 \end{array}) \times 10^{-3}$	2775	2724.0
1.45	$(2.600 \begin{array}{l} +0.062 \\ -0.067 \end{array} \begin{array}{l} +0.7 \\ -0.7 \end{array}) \times 10^{-3}$	1800	1773.7
1.55	$(1.294 \begin{array}{l} +0.039 \\ -0.043 \end{array} \begin{array}{l} +0.4 \\ -0.3 \end{array}) \times 10^{-3}$	1124	1112.3
1.65	$(5.88 \begin{array}{l} +0.23 \\ -0.26 \end{array} \begin{array}{l} +2.7 \\ -2.4 \end{array}) \times 10^{-4}$	634	635.3
1.75	$(2.27 \begin{array}{l} +0.13 \\ -0.14 \end{array} \begin{array}{l} +1.2 \\ -1.1 \end{array}) \times 10^{-4}$	318	309.3
1.85	$(6.98 \begin{array}{l} +0.67 \\ -0.69 \end{array} \begin{array}{l} +5.3 \\ -3.4 \end{array}) \times 10^{-5}$	126	119.5
1.95	$(1.89 \begin{array}{l} +0.29 \\ -0.32 \end{array} \begin{array}{l} +1.9 \\ -0.6 \end{array}) \times 10^{-5}$	43	40.8
2.05	$(5.3 \begin{array}{l} +1.4 \\ -1.6 \end{array} \begin{array}{l} +6.0 \\ -2.8 \end{array}) \times 10^{-6}$	15	14.2
2.15	$(2.5 \begin{array}{l} +0.7 \\ -1.1 \end{array} \begin{array}{l} +0.1 \\ -1.9 \end{array}) \times 10^{-6}$	9	8.5
2.25	$< 5.4 \times 10^{-7}$	0	0
2.35	$< 4.3 \times 10^{-7}$	0	0

Table VI. Correlation matrix of the spectrum accounting for systematic uncertainties.